International Journal of Aeronautical & Space Sciences (2018) 19:291–304
https://doi.org/10.1007/s42405-018-0010-x

IJASS International Journal of Aeronautical and Space Sciences

ORIGINAL PAPER

Steady Aerodynamic Characteristics of Two-Dimensional NACA0012 Airfoil for One Revolution Angle of Attack

Byung Ho Park[1] · **Yong Oun Han**[1]

Received: 20 January 2017 / Revised: 26 November 2017 / Accepted: 15 December 2017 / Published online: 6 April 2018

Abstract
Steady variations in aerodynamic forces and flow behaviors of two-dimensional NACA0012 airfoil were investigated using a numerical method for One Revolution Angle of Attack (AOA) at Reynolds number of 10^5. The profiles of lift coefficients, drag coefficients, and pressure coefficients were compared with those of the experimental data. The AERODAS model was used to analyze the profiles of lift and drag coefficients. Wake characteristics were given along with the deficit profiles of incoming velocity components. Both the characteristics of normal and reverse airfoil models were compared with the basic aerodynamic data for the same range of AOA. The results show that two peaks of the lift coefficients appeared at 11.5° and 42° and are in good agreement with the pre-stall and post-stall models, respectively. Counter-rotating vortex flows originated from the leading and trailing edges at a high AOA, which formed an impermeable zone over the suction surface and made reattachments in the wake. Moreover, the acceleration of inflow along the boundary of the vortex wrap appeared in the profile of the wake velocity. The drag profile was found to be independent of the airfoil mode, but the lift profile was quite sensitive to the airfoil mode.

Keywords Lift and drag coefficients · High Angle of Attack · Reverse airfoil mode · Reattachment

1 Introduction

To improve the performance of airfoils, the primary focus has been on improving the lift–drag ratio for very low Angle of Attacks (AOAs) before the onset of a stall in aerodynamic applications. However, the extended usage of functional wings, such as vertical-axis wind turbines, an acrobatic maneuvering plane during quick motion, and unmanned micro air vehicles, which need relatively less stability, requires rather drastic aerodynamic performance at very high AOA or even at the reverse airfoil mode. Hence, the aerodynamics at extreme high AOA including the reverse airfoil mode need to be examined.

Early investigation on aerodynamic behavior for one revolution AOA for the NACA0012 airfoil was conducted on wind turbines [1,2]. Sheldahl and Klimas provided experimental data for an 180° AOA in a vertical-axis wind turbine [1]. Spera [3] suggested model relationships of lift and drag coefficients for pre-stall and post-stall AOAs. Timmer [4] reported an integrated review based on the previous experimental data. Lee et al. [5] observed the wake characteristics for 360° AOA. Recently, Lind et al. [6] reported static aerodynamic characteristics for one revolution AOA and introduced multiple stalls at different angles including the reverse mode, which occurs in the retarding rotor blade near the root of a forward-flight helicopter.

Several theoretical and experimental studies were conducted on aerodynamic behaviors of the two-dimensional NACA0012 configured airfoils. Most of them focused on the pre-stall aerodynamics. Most two-dimensional airfoil data obtained from wind tunnels inevitably contain the corner-vortex effect, which can be ignored at pre-stall AOAs using a wing with a relatively high aspect ratio. However, the corner vortices' effect becomes substantial for short span experiments at high AOAs, because it probably results in overestimated lift and moment readings. In this study, pure aerodynamics behavior is determined numerically for both normal and reverse airfoil modes, particularly at high or extreme AOA for one revolution of the airfoil by eliminating the corner effect.

✉ Yong Oun Han
yohan@yu.ac.kr

[1] School of Mechanical Engineering, Yeungnam University, Gyeongsan 38541, Republic of Korea

2 Numerical Setup

2.1 Governing Equations

To understand the steady flow behavior around the two-dimensional airfoil including the wake region, simulations were conducted using a commercial code, FLUENT, which is based on the steady Navier–Stokes equation. Moreover, to determine the Reynolds stresses ($-\rho\overline{u_i' u_i'}$), the Spalart–Allmaras turbulence model [7] was employed, which was especially efficient to establish the drop of C_L profile in deep stall range of AOA, whereas other typical two equation models not worked properly.

The equations describing the conservations of mass and momentum, respectively, are given as follows:

$$\frac{\partial}{\partial x_i}(\rho u_i) = 0 \tag{1}$$

$$\frac{\partial}{\partial x_j}\left(\rho u_i u_j\right) = -\frac{\partial \mathrm{P}}{\partial x_i} + \frac{\partial}{\partial x_j}\left[\mu\left(\frac{\partial u_i}{\partial x_j} + \frac{\partial u_j}{\partial x_i} - \frac{2}{3}\delta_{ij}\frac{\partial u_k}{\partial x_k}\right)\right] + \frac{\partial}{\partial x_j}\left(-\rho\overline{u_i' u_j'}\right). \tag{2}$$

The transported variable in the Spalart–Allmaras model, $\tilde{\nu}$ is the modified turbulent kinematic viscosity except in the near-wall region. The following is the transport equation for $\tilde{\nu}$:

$$\frac{\partial}{\partial x_i}(\rho\tilde{\nu}u_i) = G_\nu + \frac{1}{\sigma_{\tilde{\nu}}}\left[\frac{\partial}{\partial x_j}\left\{(\mu + \rho\tilde{\nu})\frac{\partial \tilde{\nu}}{\partial x_j}\right\} + C_{2b\rho}\left(\frac{\partial \tilde{\nu}}{\partial x_j}\right)^2\right] - Y_\nu, \tag{3}$$

where u_i is velocity components ($i = 1, 2, 3$), G_ν is the production of turbulent viscosity, and Y_ν is the destruction of turbulent viscosity that occurs in the near-wall region because of wall blocking and viscous damping. $\sigma_{\tilde{\nu}}$ and $C_{2b\rho}$ are constants, and ν is the molecular kinematic viscosity. The enhanced wall treatment is not used in this study.

2.2 Computational Domain and Boundary Conditions

Figure 1 shows the geometric size of the computational domain and boundary conditions for all simulations. The chord length of the NACA0012 airfoil is a non-dimensional unit length and is situated in the center of the vertical plane. The inlet, outlet, upper, and bottom boundaries were maintained sufficiently long (30 times of the chord length), so that the boundary effects are negligible. A uniform inlet velocity of 10 m/s was set, and the Reynolds number (Re) was fixed to 1×10^5 for the calculations. The boundary conditions for the simulations were set to no-slip conditions for the surface of the airfoil and the upper and bottom domain limits ($u = v = 0$), uniform flow at the inlet boundary ($u = U, v = 0$), and pressure outlet condition at outlet boundary, respectively.

2.3 Test Case and Grid System

The hybrid unstructured grids were used for the simulations. For all the cases, the grids near the airfoil region were configured, such that y+ is less than one. To reduce the grid-interface effect, the inner unstructured region was selected within a circle of 20 times of chord length diameter. The outer region was selected using a triangular grid. Figure 1 shows the grid system, which has 200,000 elements. Moreover, to understand

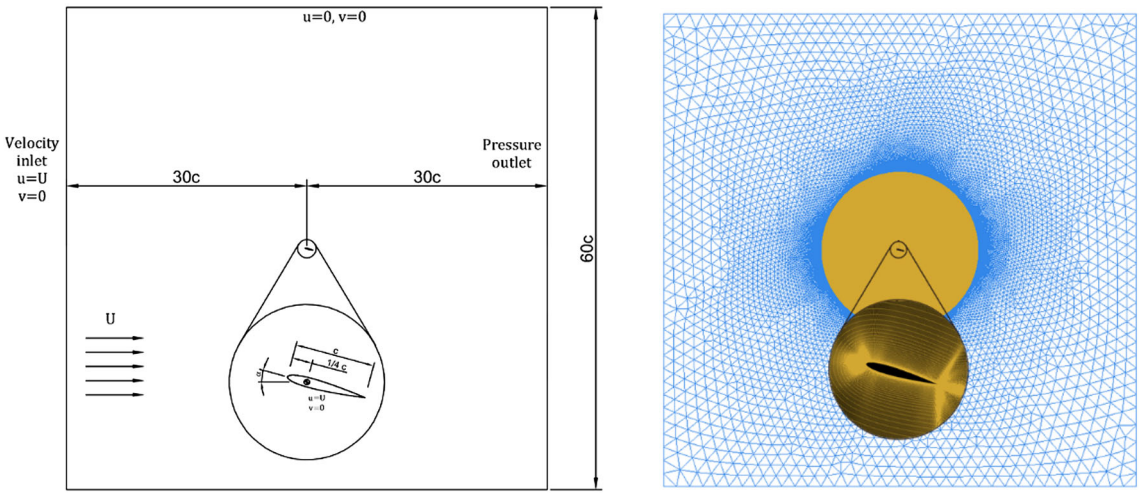

Fig. 1 Schematic of computational domain (left), grid combination of an inner unstructured grid around the airfoil, and the outer triangular grid (right)

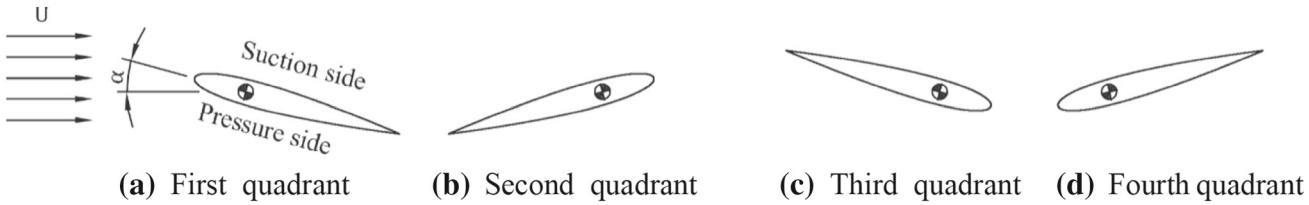

Fig. 2 Schematic of the postures of the airfoil in four sequential quadrants

the aerodynamic characteristics of the NACA0012 airfoil during one revolution, 140 AOAs were chosen unevenly. The angle grid of the AOA was chosen for every 1° near the four different stall regions and every 5° in other regions.

3 Results and Discussion

3.1 Aerodynamic Behaviors during One Revolution of AOA and Models

During one revolution of the airfoil, it experiences four different types of stalls in each quadrant. For simplicity, the airfoil modes are classified as follows: normal nose-up mode, reverse nose-down mode, reverse nose-up mode, and normal nose-down mode for sequential quadrants, respectively. Figure 2 was employed for further discussion, as it is an apt representation. For AOAs ranging from 90 to 270°, the airfoil has a sharp leading edge and a blunt trailing edge. In this particular range, for convenience, the airfoil is in the 'reverse-airfoil mode'. Note that the rotation center was fixed at the quarter chord.

The previous studies show that the profiles of the lift coefficient fairly depended on the Reynolds number, as shown in Fig. 3. With the increase in *Re*, both the first and second peaks increase, and the stalls seem to delay. Timmer [4] pointed out that in the previous experiments, the lift coefficient coincided at only three angles— 0°, 24°, and 90°—implying that consistency is hard to achieve even in two-dimensional experiments. However, it is notable that the profiles are skew symmetric with respect to 90°. Hence, the nose-down reverse airfoil mode, which is in the AOA range 90–180°, has a similar behavior as that of the first quadrant. Moreover, the magnitudes of the corresponding peaks in the reverse mode are reduced by a lesser extent than those of the first quadrant in most cases.

In this study, *Re* was selected as 1.0×10^5, which is in the practical range employed for a typical vertical-axis wind-turbine usage. It can be estimated, for example, using the following conditions: an inflow velocity of 10 m/s and a chord length of 0.15 m. The experimental results obtained from the study by Lind et al. [6] were selected as the reference data, which were obtained for

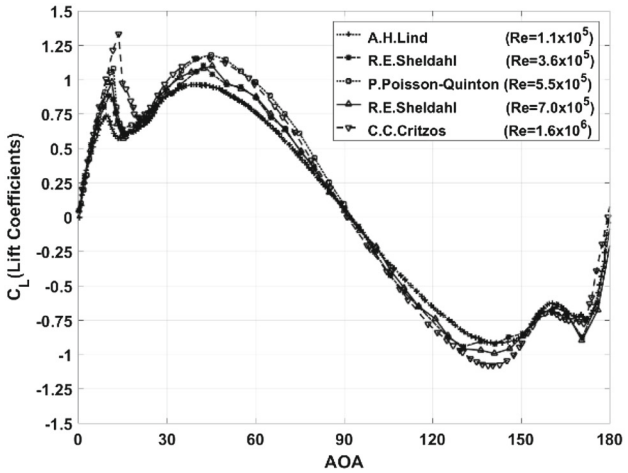

Fig. 3 Profiles of lift coefficients for the AOA range 0°–180° AOA of previous studies [4]

the closest Reynolds number with respect to this calculation.

Figure 4 shows the numerical results plotted for one-revolution AOA for lift and drag coefficients versus AOA. The profiles are compared with the experimental data obtained from the work done by Lind et al. [6]. The profile of the lift coefficient shows that angles of the first peak, the deep stall, and second peak coincided well with the experiment results. The first peak, deep stall, and second peak appear at 11.5°, 16°, and 42°, respectively. This trend is maintained for the nose-down postures of the airfoil with AOAs 315°, 344°, and 348.5°. The calculated three angles closely coincide with those of the experimental results in the first and fourth quadrants, though the magnitudes show slight discrepancies.

However, the discrepancies of magnitudes of the lift coefficients between numerical and experimental results become substantial, particularly for the reverse airfoil mode, as shown in Fig. 4. They seemed to be caused by the corner effect or corner vortex [10], which appears at the corner between the suction surface of the two-dimensional wing and wind tunnel walls, whereas the numerical results are definitely free from this corner effect. The shorter-span airfoil may cause more contamination particularly for reading the value of lift.

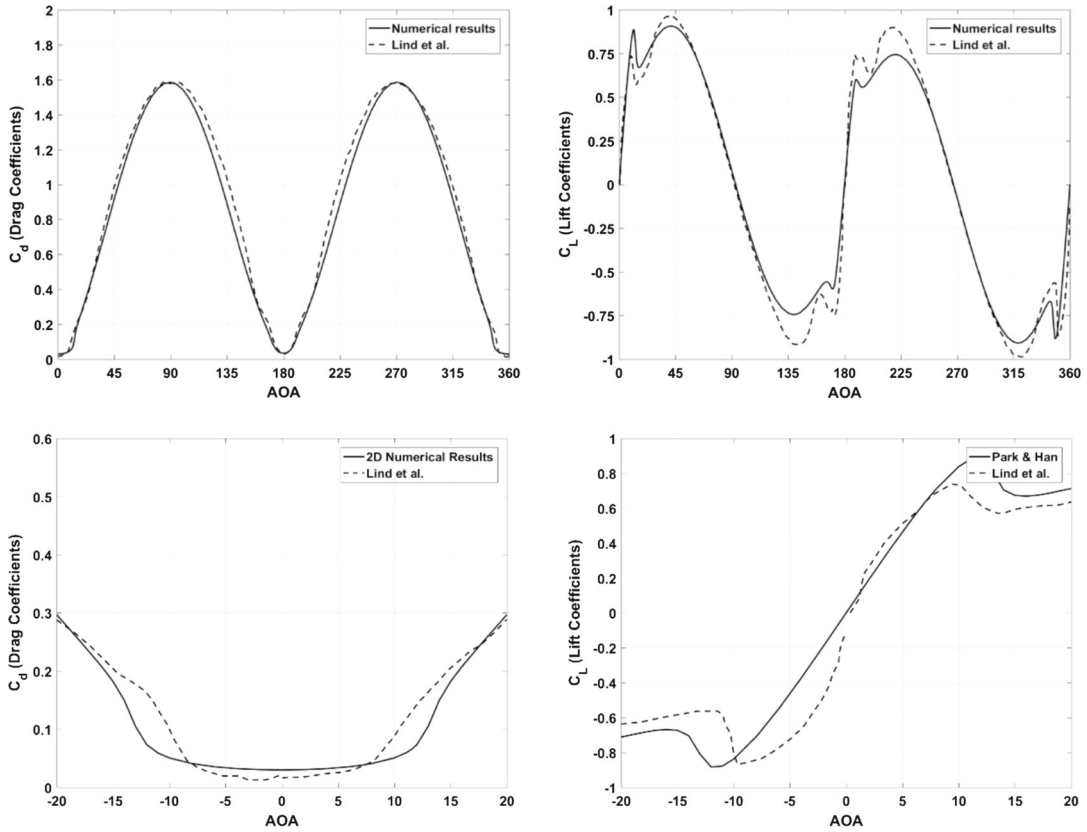

Fig. 4 Comparison of numerical profiles of drag coefficients (left) and lift coefficients (right) with the experimental data obtained from the study by Lind et al. [6]

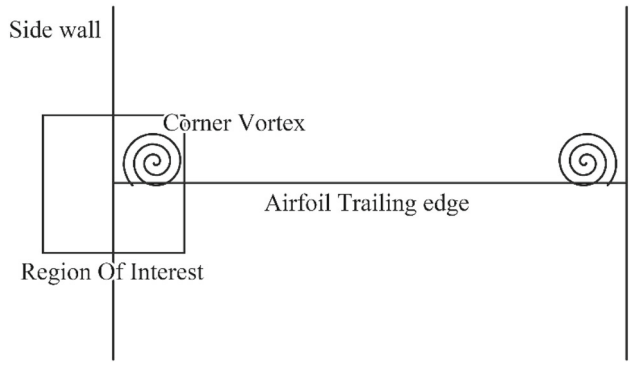

Fig. 5 Schematics of 3D corner-vortex numerical experiment

To verify the existence of the corner vortices, a short numerical 3-D experiment was carried out using an NACA0012 airfoil with aspect ratio, and ratio to chord length and span length is 4, as shown in Fig. 5, which simulates the wind tunnel experiment just like the work case by Lind et al. The numerical scheme and domain were maintained as the two-dimensional cases. Results of the pressure contours near the corner and C_L readings at 5°, 10° for the normal mode and 185°, and 195° for the reverse mode were provided in Fig. 6, respectively. These pressure contours convince the corner vortices which exist at each corners. It is acknowledged that the static pressure at the vortex center becomes negative or smallest compared to the surrounding. Moreover, the C_L readings of 3-D cases near the first peaks provide the values close to the experimental results done by Lind et al., as shown in Fig. 7. It supports that the lift coefficients of the experiment have the possibility to include the corner effects. It is not sufficient to insure that the discrepancy comes only from the corner effect with a present short 3-D numerical experiment. However, except the AoA range between two peaks for each airfoil mode, the profile of C_L reading fits well to the experimental results. Especially, the present work distinctively produces the peaks and the deep stall at the same angles as those of the experiment appeared. Therefore, it is considered that the present C_L profile represents the qualitative flow behavior well enough with respect to the angle variation.

It is also observed that the corner vortex originated from the leading-edge junction becomes strong until the AOA of the second peak. After the second peak, another corner vortex is generated at the trailing-edge corner. However, after the second peak, the split-corner vortices leave the wing surface rather immediately and become ineffective for a long time. For the reverse mode, the trailing-edge corner vortices linger

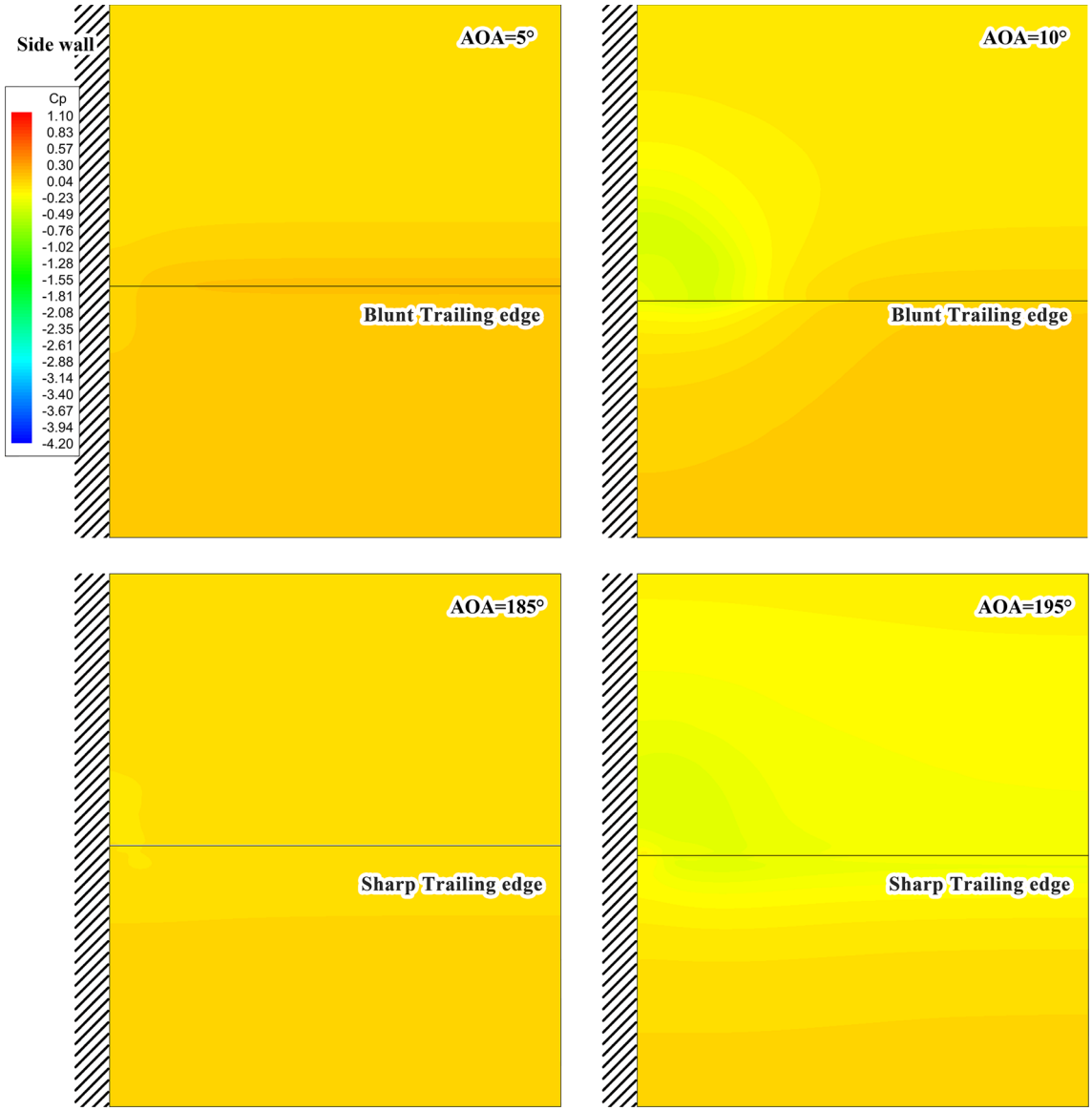

Fig. 6 Pressure contours on the vertical planes containing trailing edge at AOA of 5°, 10°, 185°, and 195°

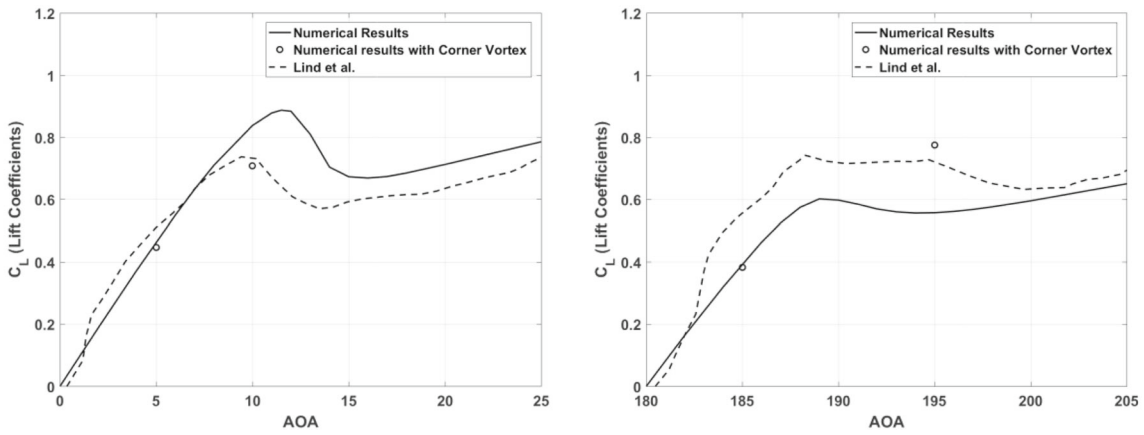

Fig. 7 Sample test for C_L readings obtained by the 2-D wing and wall geometry at 10° for the normal mode and 195° for the reverse mode, respectively

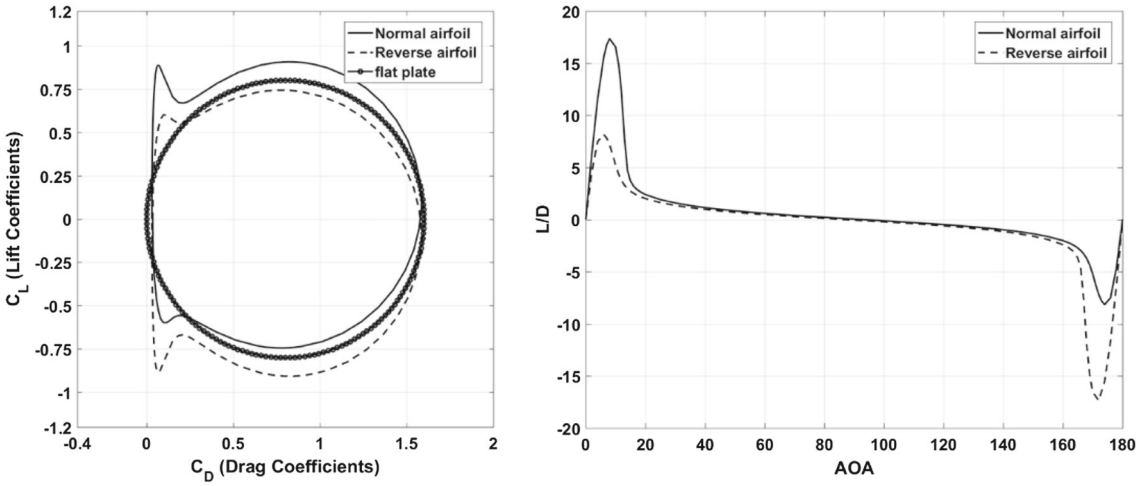

Fig. 8 Polar plot of lift coefficient versus drag coefficient (left) and ratios of *L*/*D* (right)

near the wing surface along the blunt corner and become considerably effective, causing significant discrepancies, as shown in Fig. 4.

Compared to the lift reading, the profile of the calculated drag coefficient is in good agreement with that of the experimental data, as it is relatively not affected by the corner vortices. It is noted that both the profiles have simple harmonic distributions with a period of 180°. Lee et al. [5] suggested that a flat plate, which has a theoretical zero thickness under the assumption of inviscid flow, may yield a circular polar plot for the graph of lift coefficient versus the drag coefficient with a non-dimensional radius. It is notable that the theoretical polar plot has the same magnitude of lift coefficient as that of the drag coefficient within the period of 180°. Hence, the numerical results were plotted again using Eqs. (4), (5), and (6) using the constant amplitude as suggested by Lee et al. The results are plotted in Fig. 8, including profiles of the L/D ratio:

$$C_{\mathrm{L}} = \frac{L}{\frac{1}{2}\rho V^2 c} = 0.8\sin 2\theta \tag{4}$$

$$C_{\mathrm{D}} = \frac{D}{\frac{1}{2}\rho V^2 c} = -0.8\,cos\,2\theta + 1.0 \tag{5}$$

$$\frac{(C_{\mathrm{D}} - 1.0)^2}{(-0.8)^2} + \frac{C_{\mathrm{L}}^2}{0.8^2} = \cos^2 2\theta + \sin^2 2\theta = 1. \tag{6}$$

The normal airfoil mode has a definite advantage before the first stall, showing a steep slope in the polar plot, while for the reverse airfoil mode, the maximum peak is observed at 348.5°. Except those of the first peak and the stall regions in either modes, the polar plot shows a circular profile with a radius of 0.8 and center (0.8, 0), as suggested by Lee et al. [5].

Spera suggested model equations for lift and drag coefficients by employing experimental data from various types of airfoils. Exponential functions were used by dividing one quadrant into two regions. The quadrant was divided into the pre-stall range, which includes the first peak of the lift profile, and the post-stall range with the second peak in the lift profiles. Moreover, a simple sine function was used for the drag profile, which was referred to as the 'AERODAS' model [3].

The AERODAS model introduces two different algebraic equations for the pre-stall and post-stall ranges of AOAs for the lift coefficient. In the pre-stall range, the following is the equation for the lift coefficient in the first quadrant:

$$C_{\mathrm{L}} = s\,(\alpha - A_0) - \mathrm{RC_L}\left(\frac{\alpha - A_0}{\mathrm{AC_L} - A_0}\right)^N, \tag{7}$$

where $\mathrm{RC_L} = s\,(\mathrm{AC_L} - A_0) - C_{\mathrm{L,max}}, N = 1 + \frac{C_{\mathrm{L,max}}}{\mathrm{RC_L}}$, s is the slope of the linear segment of the pre-stall curve, A_0 is the AOA at which the lift coefficient is zero at the beginning of each quadrant, $\mathrm{AC_L}$ is the AOA at the maximum lift, and $\mathrm{RC_L}$ is the reduction from extension of the linear segment of the lift curve to $C_{L,max}$. The corresponding equation for the post-stall condition is as follows.

$$C_{\mathrm{L}} = -s\,(\alpha - A_t) - \mathrm{RC_L}\left(\frac{A_t - \alpha}{A_t - \mathrm{AC_L}}\right)^N, \tag{8}$$

where $\mathrm{RC_L} = -\mathrm{s}\,(\mathrm{AC_L} - A_t) - C_{\mathrm{L,max}}$, $N = 1 + \frac{C_{\mathrm{L,max}}}{\mathrm{RC_L}}$, s is the slope of the linear segment of the post-stall curve, and A_t is the AOA at which the lift coefficient becomes zero near the end of each quadrant, precisely at 87° and 93° for the reverse and normal modes, respectively. This is because the thickness effect is different from that of a flat plate. Figure 9 shows the first and third quadrant profiles only to quantify

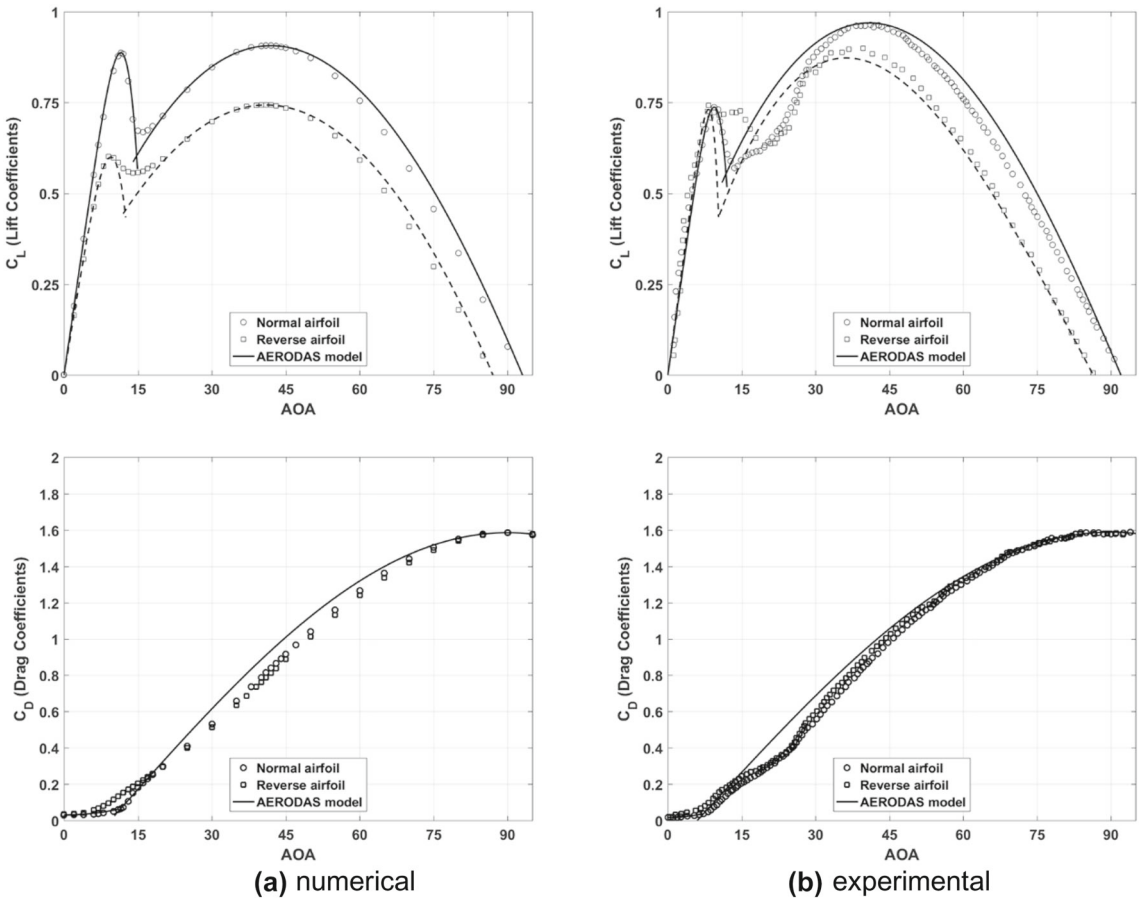

Fig. 9 AERODAS model fits for lift and drag coefficients of numerical results (left graphs) and experimental results [6] (right graphs) for both the normal and reverse modes, respectively

Table 1 Model constants for the normal mode in the four columns to the left and reverse mode in the four columns to the right

	Normal				Reverse			
	Pre-stall		Post-stall		Pre-stall		Post-stall	
	Numerical	Exp	Numerical	Exp	Numerical	Exp	Numerical	Exp
$C_{L,max}$	0.89	0.73	0.91	0.96	0.6	0.73	0.74	0.86
AOA[a]	11.5	9.42	42	41.17	9.5	8.27	41	36.78
N[b]	5.71	5.67	2.25	2.45	4.35	8.02	2.02	3.14

[a]Angle of peak values
[b]Exponent of model equation

the corner-vortex effect by observing the difference. Table 1 gives the summary of the quantifications.

The lift profiles of the reverse mode have small magnitudes at both peaks in most cases, which are 18% less averaged than those of the normal mode for both numerical and experimental results. Compared to those of the normal mode, the experimental data of the reverse mode show much deviation to the model curve. It also implies that the experimental data were contaminated by the corner effect.

Compared to the lift profiles, the drag coefficients matched well with the simple sine function, as shown in Fig. 9, for both normal and reverse modes except the pre-stall region. This result explains that with the increase in AOA, the effect of the lift reading of the reverse mode on the corner-vortex effect increases considerably, which supports the fact that the blunt rounded trailing edge of the reverse airfoil has more corner effect as observed earlier. However, it is noticeable that the drag readings of both the modes coincide well with each other for both the experiment and numerical analyses. This behavior of the drag profiles will be further examined again in the later.

3.2 Steady Vortices and Flow Patterns

To observe the flow patterns around the airfoil, some streamlines in proximity to the airfoil were drawn at specified AOAs of 11°, 16°, 42°, and 90° for the normal airfoil mode and 191°, 196°, 222°, and 270° for the reverse mode. The specified AOA selected symmetric AOA based on the first peak, the deep stall, and the second peak appear.

The flow patterns are shown in sequential plots including contours of the static pressure and profile of the pressure coefficient at corresponding angles for the normal mode, as shown in Fig. 10. As seen in the figure for the pre-stall angles, the streamline does not have any drastic change in pattern, but the leading-edge steady vortex roll (hereafter LEV for convenience) was clearly observed for a deep stall angle of 16°; during the post-stall, the counter-rotating trailing-edge steady vortex roll (TEV in short) showed off. The stall flow was separated near the leading edge, as expected, and a considerably steady vortex roll up was observed, making the streamlines of the inflow push up along the suction surface. By observing the magnified trailing region, a slight counter-rotating TEV starts at the deep stall. As the TEV lingers on the very end suction surface near the trailing edge, it stimulates the stall by making LEV stay longer on the suction surface. Thereafter, the TEV becomes stronger, creeping forward direction in a short distance on the suction surface. At an AOA of 42°, the lift coefficient builds the second peak and has uneven strength vortex pair in wake, similar to the ones observed behind the blunt body. At 90°, almost evenly paired vortices were established similar to the ones observed behind the vertical flat plate. It is easily anticipated that the streamlines of the incoming flow were not seemed to penetrate into the zone of these steady vortex pairs on the suction side of the airfoil, and the boundary of this zone acts like the dividing line in the potential flow analysis. Such an observation is quite different from the unsteady case, which is basically investigated by tracking the vortex roll up [8].

Based on the attached profiles of the static pressure coefficients around the airfoil, the pressure difference between the suction and pressure surfaces becomes maximum near the leading edge for an AOA of 11°, which induces the first peak of the lift profile. During the post-stall, the static pressure over the suction surface becomes rather constant because of the vortex mixes. It is noted that even on the pressure side, the static pressure has a negative maximum for the post-stall angles, because the flow is accelerated around the leading edge.

The coefficient profiles show that the reverse airfoil mode has lower lift value than that of the normal airfoil in the first quadrant revolution of AOA, while it has comparable value of drag except for the pre-stall range of AOA, as shown in Fig. 11. To compare the aerodynamic characteristics of the reverse airfoil mode to those of the normal mode, four angles 191°, 196°, 222°, and 270° were selected corresponding to angles 11°, 16°, 42°, and 90° of the normal mode. Their results are plotted in Fig. 12 with profiles of the pressure coefficients. As shown in this figure, the reverse airfoil shows a stall with lower maximum lift coefficient. However, the stall takes place slightly earlier, as the streamline at 191° already starts to roll, because it is separated from the sharp leading edge. The steady roll of the line vortex looks similar to those of the normal mode afterwards.

As seen in the streamline shape even at an angle of 191°, the reverse airfoil already entered the leading-edge separation, whereas the normal airfoil did not yet start. The pressure distribution supported this early separation, as shown in Fig. 12, wherein the suction surface pressure was flattened because of the vortex mixing action similar to the behavior observed at higher angles. This supports the strength of the corner vortices owing to the reverse airfoil developed more active than those of the normal airfoil and, therefore, explains the corner effect became more substantial in lift force measurement, which induced overestimated as observed in Fig. 2.

The reverse airfoil experiences a nose-up moment in the whole range, 0°–90° of AOA, while the normal airfoil experiences a nose-down moment in most range except low AOA, as shown in Fig. 13. This may be easily explained by recognizing that the rotation center locates at 1/4c for the normal airfoil and at 3/4c for the reverse airfoil. In C_M profile of the reverse airfoil, a sudden decrease appeared in the AOA range of 191°−196°, which was caused by the turnover of the static pressure distribution near the rotation center of the reverse airfoil, as shown in Fig. 13. In higher AOA range, the blunt trailing edge induces earlier acceleration even on the pressure side near the trailing edge, which stimulates a considerable counter-rotating TEV, as shown in Fig. 13.

Hence, the vortex pairs generated by the LEV and TEV, counter rotating to each other, form an impermeable space over the suction surface and divide the flow field into detouring and circulating flow regions, respectively. It is interesting to examine the size of the circulating region at high AOA. To observe the evolving structure with AOA, it is convenient to determine the location of the reattachment end point of both vortices, which is one of the frequent methods used in the annular jet [9]. At the reattachment point, the local stagnation velocity is generated because of the counter-rotating vortices, as seen in the exaggerated view of 42° case in Fig. 14. The figure shows the movement of the stagnation points with AOA for both normal and reverse modes obtained from 17 different AOA cases. It is noted that two-dimensional fairing generated by the vortex pairs increases with AOA, thereby developing an effective thick airfoil eventually. The interaction of both the vortices causes a drastic aerodynamic behavior.

The graph on the right of Fig. 14 shows the movement of the reattachment point with respect to AOA. At an AOA of 14°, the reattachment can be measured, as the two vor-

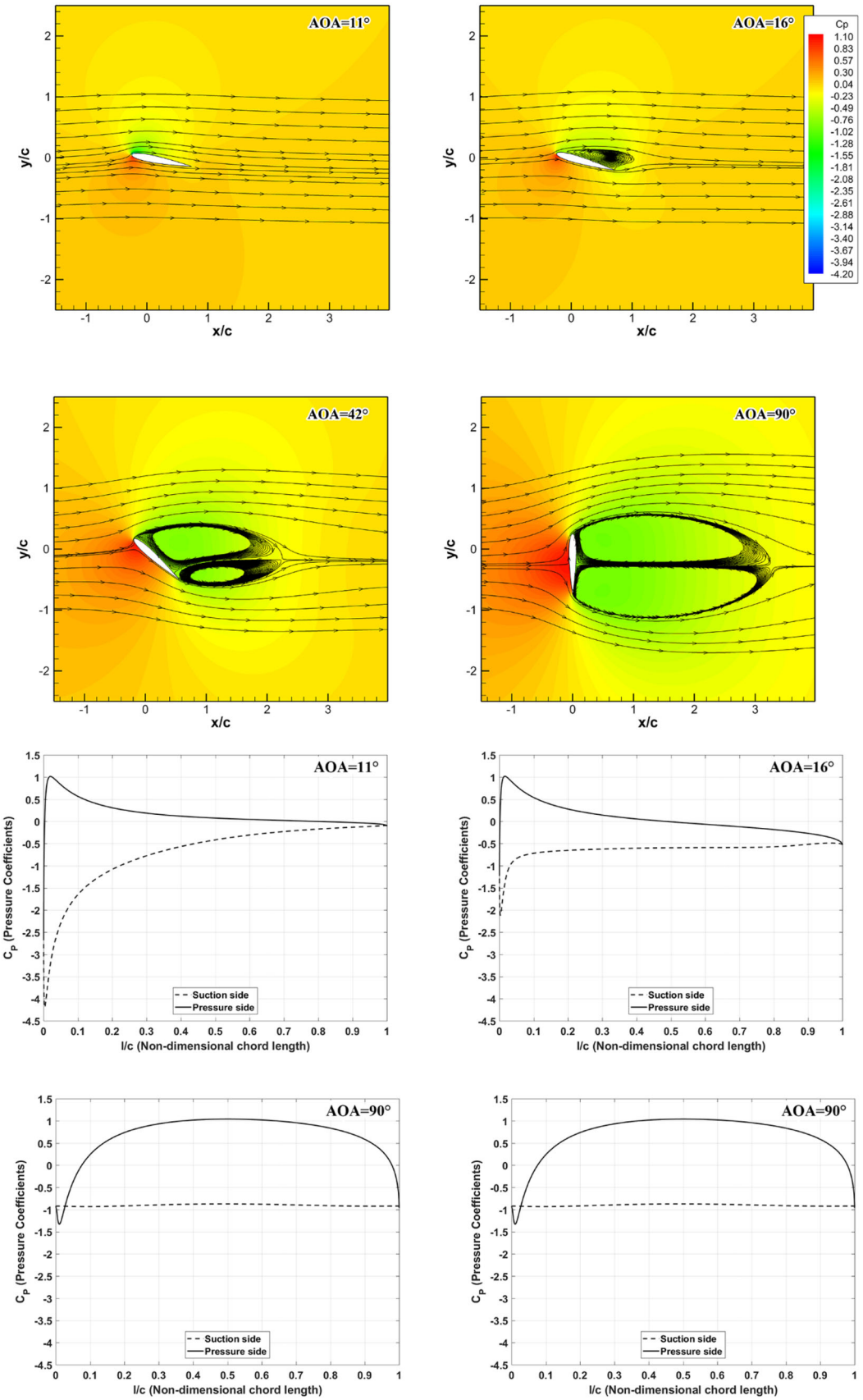

Fig. 10 Streamlines, vortex pairs, and profiles of the pressure coefficients of the normal airfoil mode for AOAs of 11°, 16°, 42°, and 90°

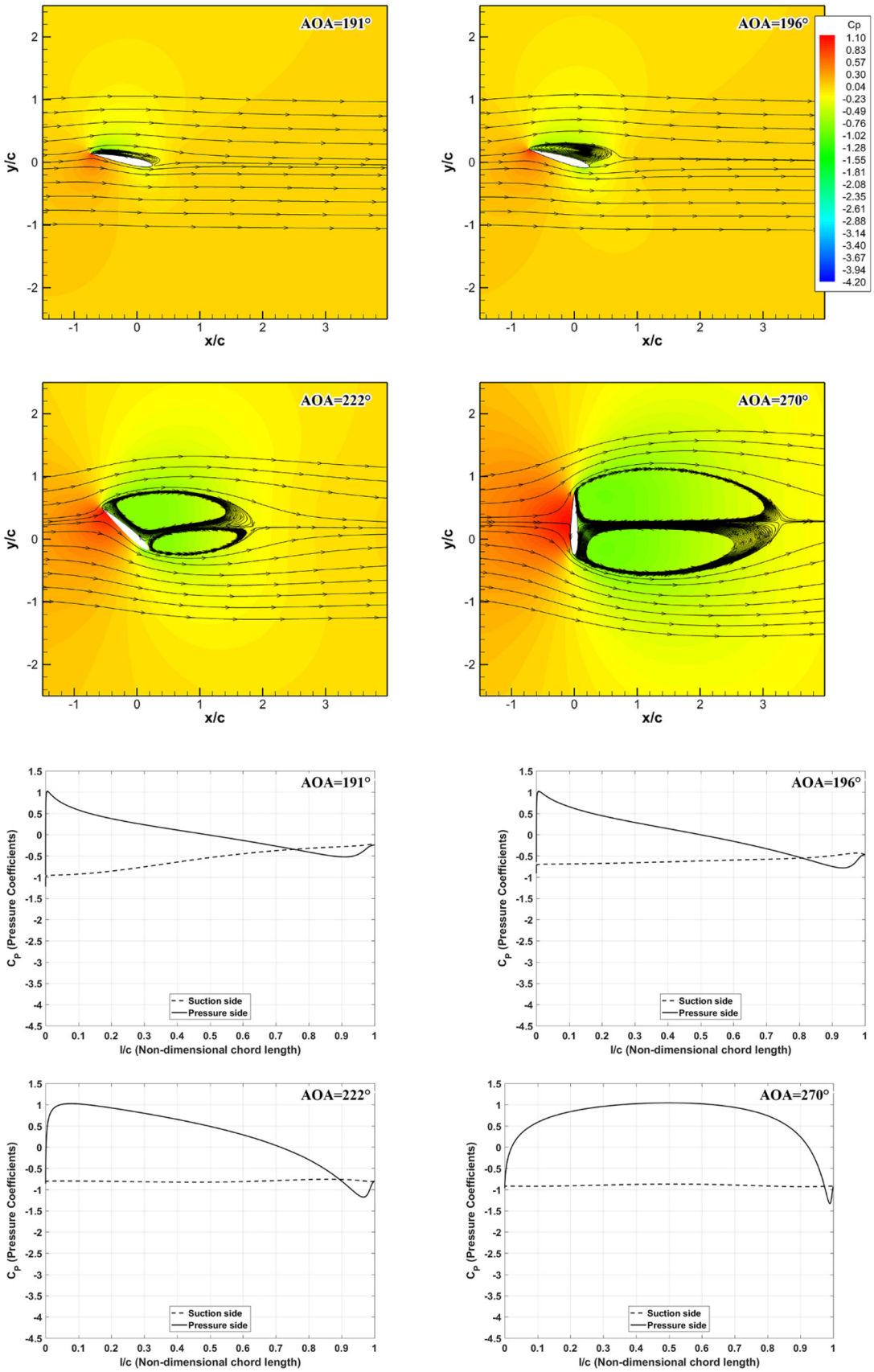

Fig. 11 Streamlines, vortex pairs, and profile of pressure coefficients for the reverse airfoil mode at AOAs of 191°, 196°, 222°, and 270°

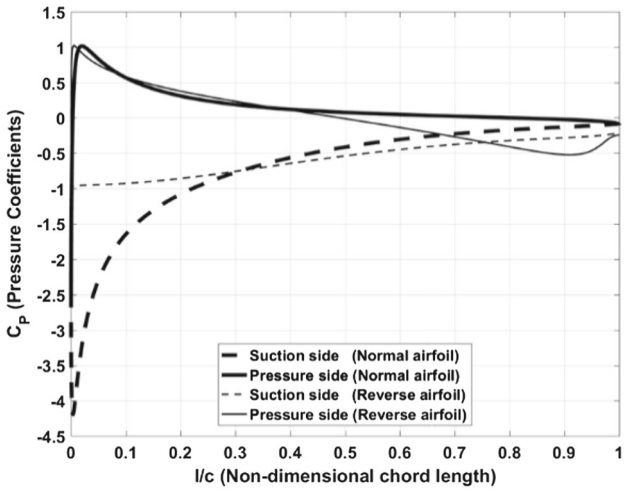

Fig. 12 Pressure profiles at deep stall angles of 11° and 191° for the normal and reverse modes

tices become visible in the streamline. At the case of 90 of AOA, the reattachment end of the normal mode reaches to the maximum, 3.3 times the chord length downstream, and stays a little bit below the horizontal plane which includes the rotation center as shown in the figure right. However, for the reverse mode, the maximum reattachment end locates above the horizontal plane with the same maximum size. Hence, it seems that the reverse mode airfoil pushes up the vortex wrap because of the flow acceleration along the blunt curved contour along its trailing edge.

3.3 Wake Velocity and Local Accelerations

The profile of the wake velocity provides the following information about an airfoil: velocity deficit, profile drag, wake region, and even wake form. Figure 15 shows the comparison of the numerical velocity profiles obtained at

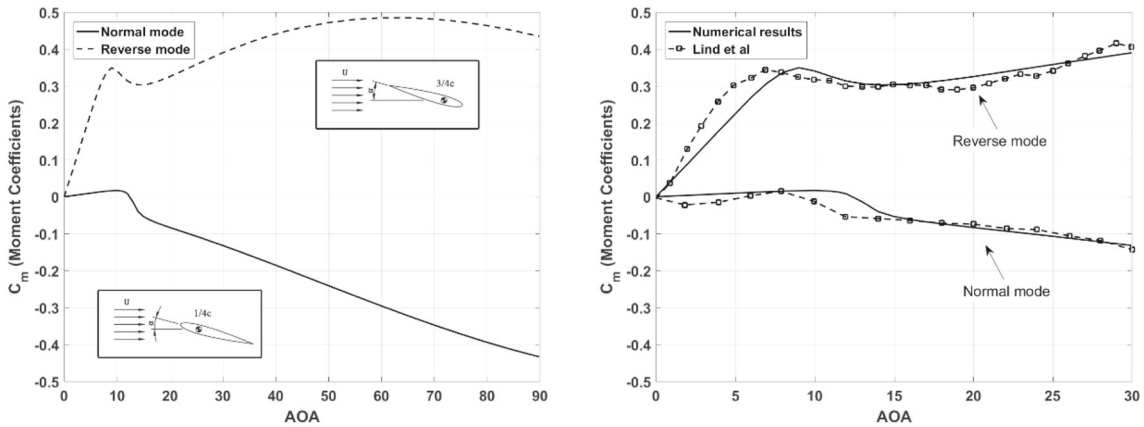

Fig. 13 Moment coefficients of normal airfoil and reverse airfoil in 0 ∼ 90 AoA range, and comparison to experiment (Lind et al.)

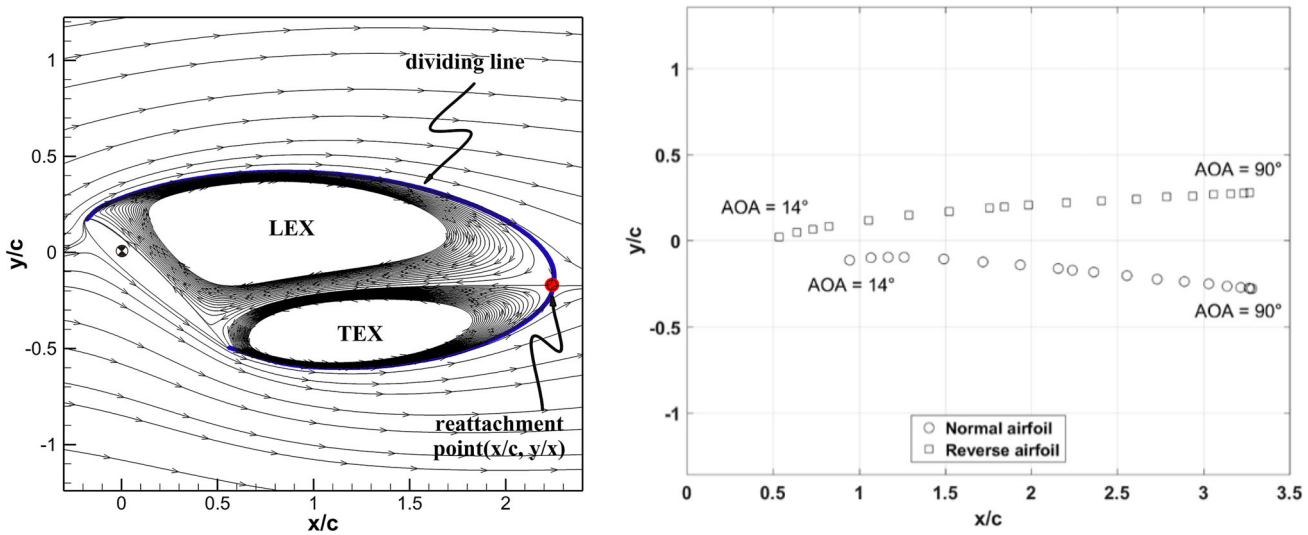

Fig. 14 Schematic diagram of reattachment point at an AOA of 42° (left), reattachment point tracking of normal and reverse airfoil modes in the first quadrant (right)

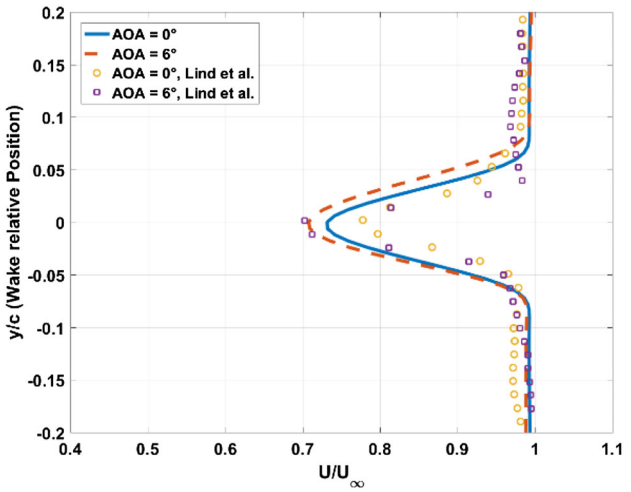

Fig. 15 Velocity defects at 1.4 times chord length downstream for AOAs of 0° and 6°

1.4 times the chord length downstream for AOAs of 0° and 6° with those of Lind's experimental data. At zero angle posture of the airfoil, the calculated velocity profile matched well with the experimental data, showing a relevant symmetry with a proper deficit. For the case wherein the AOA is 6°, both have the same deficit, but a sign of acceleration near upper wall was detected with a rather narrower width of deficit profile of the experiment. It was interesting to observe how the acceleration develops with AOA.

The wake characteristics behind the airfoil can be better understood using mean velocity profiles. Figure 16 shows the wake velocity profiles at several downstream positions for given AOAs. These plots show velocity deficit and acceleration behind the airfoils. The origin of abscissa was chosen at 1/4 chord at which the airfoil rotates. It is noted that once the dividing line built, the inflow near its boundary becomes faster than the incoming velocity, so that it results in acceleration around the fairing induced by both vortex wraps. This acceleration observed in the wake profile was also detected in Lind's experimental data at zero AOA as mentioned previously. At 42°, the acceleration becomes substantial as shown in this figure. Hence, around the post-stall angle, the fairing effect prevails, as observed before in Fig. 14.

The inflow velocity acceleration becomes active as AOA increases, and the local velocity increases as much as 1.3

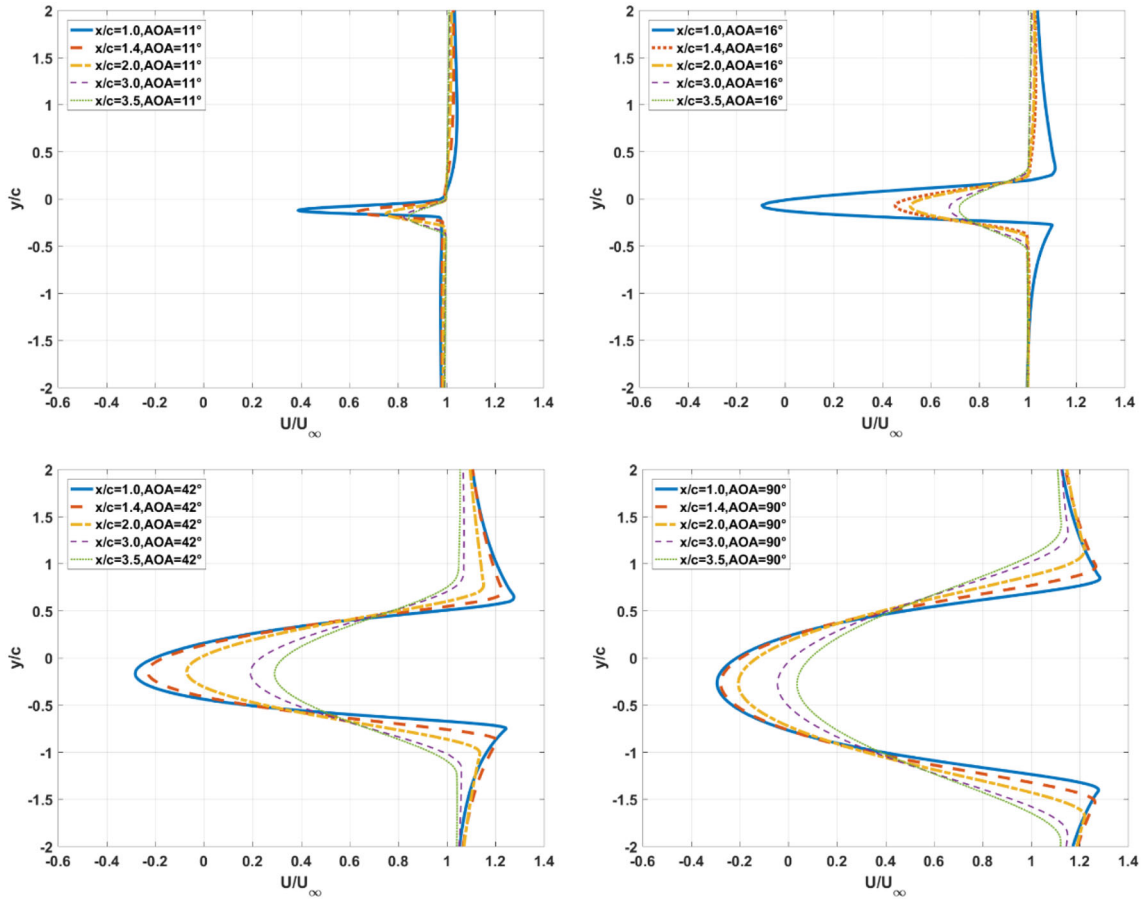

Fig. 16 Velocity profiles in the wake range of 1.0–3.5 times chord length for AOAs of 11°, 16°, 42°, and 90°

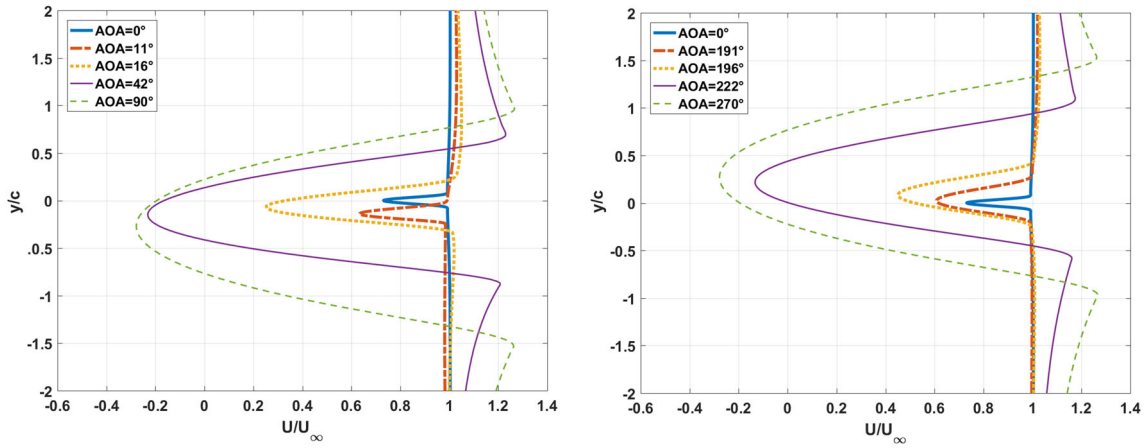

Fig. 17 Inflow acceleration profiles obtained at 1.3 times chord length downstream for the normal (left) and reverse (right) modes, respectively

times of the inflow velocity, which is the maximum. By the action of the vortex wrapping, the maximum velocity deficit near the center, which is not exactly at the center, reaches to negative 0.3 of the inflow velocity at an AOA of 90°, as shown in Fig. 16. The profiles of the wake velocities show that the vortex wrap extended to 1.1 chord length downstream for an AOA of 16°, 2.2 chord length for 42°, and 3.2 chord length for 90°. The acceleration will be sustained for a while, as the reattachments were established by both the vortices. For the reverse mode, similar behaviors were observed except that the velocity center moves upward, while the normal mode moves down similar to a mirror image. It implies that both modes provide the same patterns for the velocity deficit, and hence, the geometry of the trailing edge is not important for establishing the wake pattern. This is assured by the results rearranged of inflow accelerations for both modes at 1.3 times chord length downstream from the rotating center, as shown in Fig. 17.

As observed in this figure, the velocity profiles of the reverse mode at 191° show more deficit than those of the corresponding normal mode. This fact explains the reason why the drag force of the reverse mode does not provide any advantage even in the pre-stall angles compared to the normal mode, as shown in the graph to the right of Fig. 9. The drag coefficients of both airfoil modes are plotted in Fig. 18 in the AOA range of 0°–20°. Before the stall, the skin drags of both airfoils were comparable to the pressure drags. However, the pressure drag of the reverse mode becomes rapidly dominant near the stall range resulting to increase the total drag, while the pressure drag of the normal mode is still comparable to the skin drag maintaining the lower level of the total drag than the reverse mode. This is the reason why the reverse mode has more momentum deficit near the 191°. Note that the skin drag become meaningless after 20°, so that the pressure drag becomes dominant for both modes.

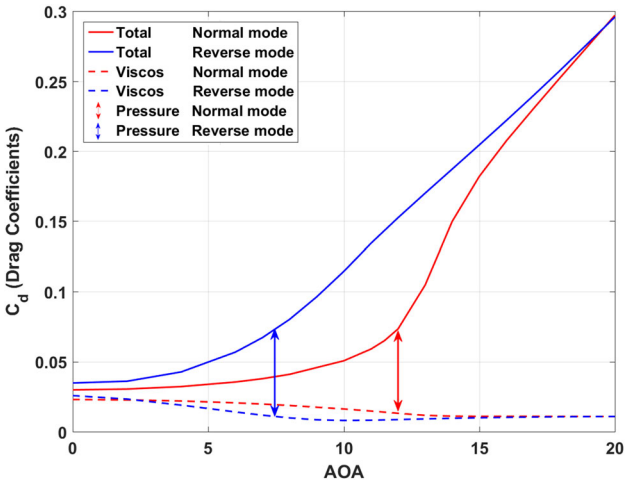

Fig. 18 Composition of the total drag near the stall range of AOA for both airfoil modes

4 Conclusions

The aerodynamic forces and flow behaviors of the two-dimensional wing which has the NACA0012 section were examined by a numerical calculation at 100,000 of *Re*. No. The investigation was also made for both normal and reverse-airfoil modes. As the results, the following conclusions have been drawn:

Three critical angles of the first peak, deep stall, and second peak in the profile of the lift coefficient were found at AOAs of 11.5°, 16°, and 42°, respectively. A substantial discrepancy in the lift reading was observed between previous experiments and the calculations in the present study. This implies that at post-stall, the experimental data were affected by the corner vortex generated at the junction of the wing and the tunnel wall, which increases the lift.

The polar plot obtained from the lift and drag coefficients closely represented a circle with a radius of 0.8 and center

at (0.8, 0). The profiles for the lift coefficients of both the normal and reverse modes matched well with the AERODAS model with the averaged $C_{L,max}$ of the reverse mode being 18% less than that of the normal mode. For high AOA, experimental $C_{L,max}$ values are higher than those that were calculated numerically in both the modes, which supported the fact that the experimental results were affected by corner vortices.

During the stall, the trailing-edge vortex was generated with a counter-rotating motion with respect to the leading-edge vortex, which increases up to an AOA of 90°. After 42°, both the vortices showed strengths comparable to each other, thereby detouring the incoming flow. Hence, the acceleration reached a value 1.3 times of the inflow velocity, and the vortex fairing was extended 3.3 chord length downstream for the maximum size.

The vortex roll-ups of the LEV and TEV on the suction surface showed an almost similar action for both the normal and reverse modes of the airfoils. This shows that the drag profiles are independent of the modes, whereas the lift profiles are very sensitive to the mode. However, the reverse airfoil provided nose-up moment, because the local static pressure becomes negative after the maximum thickness position of the airfoil, even on the pressure surface near the trailing edge.

Acknowledgements This work was supported by the 2014 Yeungnam University Research Grant.

References

1. Sheldahl Robert E, Klimas Paul C (1981) Aerodynamic characteristics of seven symmetrical airfoil sections through 180-degree angle of attack for use in aerodynamic analysis of vertical axis wind turbines. No. SAND-80-2114. Sandia National Labs., Albuquerque, NM (USA). https://doi.org/10.2172/6548367
2. Sheldahl Robert E, Klimas Paul C (1981) Aerodynamic characteristics of seven symmetrical airfoil sections through 180-degree angle of attack for use in aerodynamic analysis of vertical axis wind turbines. No. SAND-80-2114. Sandia National Labs., Albuquerque, NM (USA). https://doi.org/10.2172/6548367
3. Spera David A (2008) Models of lift and drag coefficients of stalled and unstalled airfoils in wind turbines and wind tunnels
4. Timmer WA (2010) Aerodynamic characteristics of wind turbine blade airfoils at high angles-of-attack. European Wind Energy Association
5. Lee EH, Park BH, YO Han, Kim J-H (2012) Investigation on aerodynamic behaviors at the extreme angle of attack of two-dimensional wing. In: 30th AIAA applied aerodynamics conference. p 3020. https://doi.org/10.2514/6.2012-3020
6. Lind Andrew H, Lefebvre Jonathan N, Jones Anya R (2014) Time-averaged aerodynamics of sharp and blunt trailing-edge static airfoils in reverse flow. AIAA J 52(12):2751–2764. https://doi.org/10.2514/1.j052967
7. Spalart PR, Allmaras SR (1992) A one-equation turbulence model for aerodynamic flows. In: 30th aerospace sciences meeting and exhibit. https://doi.org/10.2514/6.1992-439
8. Spalart Philippe R, Rumsey Christopher L (2007) Effective inflow conditions for turbulence models in aerodynamic calculations. AIAA J 45(10):2544–2553. https://doi.org/10.2514/1.29373
9. Im Hongsik, Zha Gecheng (2011) Delayed detached eddy simulation of a stall flow over NACA0012 airfoil using high order schemes. In: 49th AIAA Aerospace Sciences Meeting including the New Horizons Forum and Aerospace Exposition. https://doi.org/10.2514/6.2011-1297
10. Ko NWM, Chan WT (1978) Similarity in the initial region of annular jets: three configurations. J Fluid Mech 84(04):641–656. https://doi.org/10.1017/s0022112078000397
11. Harvey Neil W (1999) Non-axisymmetric turbine end wall design: Part I-three-dimensional linear design system. ASME, 1999 International Gas Turbine and Aeroengine Congress and Exhibition. Am Soc Mech Eng. https://doi.org/10.1115/99-gt-337
12. Milne-Thomson Louis Melville (1968) Theoretical hydrodynamics. Courier Corporation. https://doi.org/10.1007/978-1-349-00517-8
13. Reference Manual, FLUENT17, "Turbulence Modeling"